LARGE EDDY SIMULATION OF THE FLOW PAST AN INCLINED PROLATE SPHEROID

N. Wikström, U. Svennberg, N. Alin & C. Fureby
Dept. of Weapons and Protection, Warheads and Propulsion,
The Swedish Defence Research Agency, FOI, SE-172 90, Stockholm, Sweden
niklas.wikstrom@foi.se, urban.svennberg@foi.se,
niklas.alin@foi.se, fureby@foi.se

ABSTRACT

The presented paper concerns the application and validation of Large Eddy Simulation (LES) for the prediction of the flow around a prolate spheroid at different angles of attack. The objective is to evaluate the applicability of LES for practically relevant high Re-number flows, to study the influence of subgrid modeling and grid resolution on the quality of the results and to discuss and compare the flow and turbulence dynamics. The LES' use different subgrid and wall-models and are performed on different grids in appropriate combinations. Simulations are performed at α=10° and 20° angle of attack, and comparison with experimental data is carried out for both pressure and velocity. Reasonable agreement is found for both angles of attack, and the influences of resolution and subgrid model are both comparatively small.

INTRODUCTION

Flows around ships, submarines, and other underwater vehicles are usually quite complicated and fully three-dimensional (3D). Besides being an important feature in submarine and ship hydrodynamics, 3D open flow separation occurs in aerodynamic applications, such as the flow over cars and high-speed trains, and provides a challenge to all Computational Fluid Dynamic (CFD) models.

Traditional CFD approaches using Reynolds Averaged Navier-Stokes (RANS) models (Wilcox, 1998) and advanced steady state flow codes are often acceptable for flows not dominated by large-scale flow dynamics. A more viable approach is Large Eddy Simulation (LES) in which the large energy-containing scales of motion, that are responsible for most of the momentum transport, are solved for, whereas the small-scale turbulence is modeled (e.g. Ferziger, 1983, Sagaut, 2001 and Fureby, 2001),

This paper concerns the application and validation of LES for the prediction of boundary layer flow with complex 3D open separation and vortex formation. The subject is a prolate spheroid, with 6:1 (major-minor) semi-axis ratio at two angles of attack α. The resulting flow field is well-defined and relatively simple, but exhibits all the fundamental transition and separation phenomena of 3D flows. As shown in figure 1 the flow separating from the sides of the body rolls-up into two strong vortices trailing along the back, followed by reattachment at the centerline on the leeward surface. A second vortex structure is formed beneath each primary vortex, downstream to be entrained into the primary vortices. The boundary layer profiles are strongly affected by the separation and vortex systems and display the quality of the solution at comparison to experimental data.

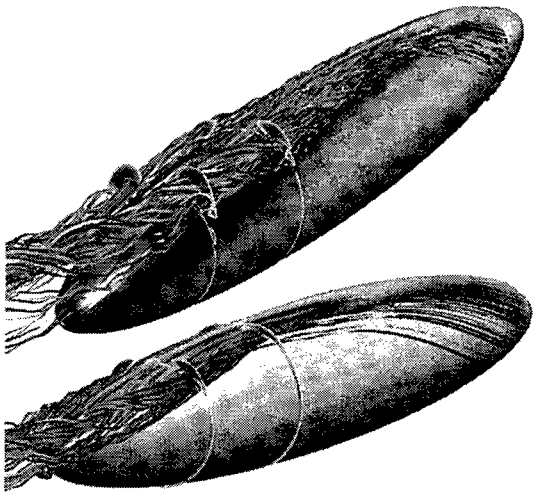

Figure 1. Perspective views of the flow in terms of streamlines, rms pressure on the hull and contours of vorticity at x/L=0.600 and 0.772. The upper panel shows the α= 20° case and the lower panel the α=10° case.

The simulations are assessed via comparison with experimental measurements from previous investigations of this flow by Chesnakas & Simpson (1996) and Wetzel *et al.* (1998), and also with the experimentally-based visualization studies of Han & Patel (1979) and Goody *et al.* (1998) providing a detailed understanding of the surface flow pattern. Due to the wealth of experimental data available and the simplicity of the geometry, this flow field has made an excellent test case for CFD models (e.g. Tsai & Whitney, 1999, Rhee & Hino, 2000, Hedin *et al.*, 2001 and Constantinescu *et al.*, 2002).

The present study is part of an ongoing research program with the long-term objective of developing a LES capability with the ability to simulate high Re-number flows of practical relevance. Future studies of this case will include examination of the predictive capabilities of the present LES models during transient maneuvers. Fur-

ther validation of separation prediction is also deemed important.

PROLATE SPHEROID CONFIGURATION

The 6:1 ellipsoid measures L=1.37 m in length, has a diameter of D=0.23 m and is sting-mounted in the Virginia Tech. wind tunnel (e.g. Chesnakas & Simpson, 1996, Wetzel *et al.*, 1998 and Goody *et al.*, 1998) having a 1.8×1.8 m^2 cross-section. The blockage is about 1.3%. The freestream velocity is v_0=46 m/s, giving a body-length Re-number of $Re_L=4.6\cdot10^6$, and a freestream turbulence intensity of I≈0.1%. In the laboratory experiments a trip-wire is mounted on the forebody at x/L≈0.2, where x denotes the distance from the nose of the ellipsoid. The available data (e.g. Chesnakas & Simpson, 1996, Wetzel *et al.*, 1998 and Goody *et al.*, 1998) includes velocity, surface pressure, rms-pressure fluctuations, boundary layer properties etc. for angles of attack between α=5° and α=30°.

The computational domain is bounded by the ellipsoid surface and by the inlet and outlet boundaries fitted to a sphere with a radius twice the body length. Thus, the domain does not take the wind tunnel walls and the blocking effects into account. These are however deemed negligible in comparison to the benefits gained from the high quality grid resulting from the chosen domain geometry. The tail mounted strut, supporting the body in the experiments is equally neglected. The domain is discretised with a block structured mesh, supported by a double O-shaped block structure, in which the inner blocks wraps closely around the ellipsoid body, making clustering of grid points toward the ellipsoid surface effective. Three meshes are used in the computations in order to parameterize the effects of the grid resolution and of the boundary layer resolution. Mesh A has ~$0.75\cdot10^6$ cells and $y^+\approx25$, where $y^+=u_\tau y/\nu$ is the non-dimensionalized distance to the wall with u_τ being the friction velocity. Mesh B is topologically similar to mesh A but with ~$1.40\cdot10^6$ cells and $y^+\approx15$. Mesh C is refined to ~$1.40\cdot10^6$ cells but all added cells are contained in the inner O-grid and the refinement is performed in the normal direction only resulting in a well resolved boundary layer having $y^+\approx5$.

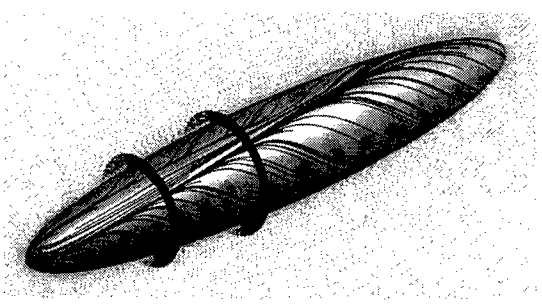

Figure 2. Schematic of the mesh and the surface flow pattern. In addition, we have included the measurement planes used for comparison with the laboratory data.

On the semi-spherical inlet boundary, Dirichlet conditions for velocity and turbulent properties and homogeneous Neumann condition for pressure are applied. The outlet boundary is fitted with a Dirichlet condition for the pressure, and homogeneous Neumann conditions for all other dependent variables. At the hull surface homogeneous Neumann conditions are used for all variable except for the velocity that is constrained by a no-slip condition.

THE LARGE EDDY SIMULATION MODEL

The fluid dynamic model used is based on the incompressible Navier Stokes Equations (NSE), describing conservation of mass and balance of momentum of an incompressible linear viscous fluid. In LES the motion is separated into small and large eddies and equations are solved for the latter. The separation is achieved by means of a low-pass filter (e.g. Sagaut, 2001). The filter is applied by convolving the flow variables with the kernel $G=G(\mathbf{x},\Delta)$, where Δ is the filter width, to extract the large scale components. Filtering the NSE yields,

$$\begin{cases}\nabla\cdot\bar{\mathbf{v}}=m^\rho,\\ \partial_t(\bar{\mathbf{v}})+\nabla\cdot(\bar{\mathbf{v}}\otimes\bar{\mathbf{v}})=-\nabla\bar{p}+\nabla\cdot(\bar{\mathbf{S}}-\mathbf{B})+\mathbf{m}^v,\end{cases} \tag{1}$$

where $\bar{\mathbf{v}}$ is the velocity, $\bar{p}$ the pressure, $\bar{\mathbf{S}}=2\nu\bar{\mathbf{D}}$ the viscous stress tensor, $\mathbf{D}=\frac{1}{2}(\nabla\bar{\mathbf{v}}+\nabla\bar{\mathbf{v}}^{\mathrm{T}})$ the rate-of-strain tensor, ν the molecular viscosity, $\mathbf{B}=\overline{\mathbf{v}\otimes\mathbf{v}}-\bar{\mathbf{v}}\otimes\bar{\mathbf{v}}$ the subgrid stress tensor, $m^\rho=[G*,\nabla]\mathbf{v}$ and $\mathbf{m}^v=[G*,\nabla](\mathbf{v}\otimes\mathbf{v}+p\mathbf{I}-\mathbf{S})$ the commutation errors, in which $[G*,\nabla]f=\overline{\nabla f}-\nabla\bar{f}$. Only the resolved scales are thus retained, whereas the subgrid scale flow physics is grouped into $\mathbf{B}$, m^ρ and $\mathbf{m}^v$. Traditionally we neglect m^ρ and $\mathbf{m}^v$ and concentrate the modeling efforts on $\mathbf{B}(\mathbf{x},t)=\mathbf{B}[\bar{\mathbf{v}}(\mathbf{x}',t');\mathbf{x},t]$. Different modeling concepts exists (Sagaut, 2001, Fureby 2001, and Fureby *et al.*, 2003), but here we focus on conventional functional models in which $\mathbf{B}$ is parameterized in terms of the subgrid kinetic energy k, the subgrid eddy-viscosity ν_k and the rate-of-strain $\bar{\mathbf{D}}$, viz.,

$$\mathbf{B}=\tfrac{2}{3}k\mathbf{I}-2\nu_k\bar{\mathbf{D}}_D \quad \text{where} \quad \nu_k=c_k\Delta k^{1/2}, \tag{2}$$

In the One Equation Eddy Viscosity (OEEVM) model (cf. Schumann, 1975) k is obtained from,

$$\partial_t(k)+\nabla\cdot(k\bar{\mathbf{v}})=2c_k\Delta k^{1/2}\|\bar{\mathbf{D}}\|^2+\nabla\cdot(\nu\nabla k)+c_\varepsilon k^{3/2}/\Delta, \tag{3}$$

where $\varepsilon=c_\varepsilon k^{3/2}/\Delta$ is the dissipation. Assuming equilibrium (3) simplifies to $k=c_I\Delta^2\|\bar{\mathbf{D}}\|^2$ from which the Smagorinsky (SMG) model $\nu_k=c_D\Delta^2\|\bar{\mathbf{D}}\|$ (Smagorinsky, 1963) results. Values of the coefficients c_k and c_ε (or c_I and c_D) can be obtained either from a $|\mathbf{k}|^{-5/3}$ inertial sub-range behavior or from a dynamic procedure as part of the solution (Germano *et al.*, 1994 and Kim & Menon, 1994).

LES of wall bounded flows becomes prohibitively expensive at high Re if one attempts to resolve the small but dynamically important eddies in the near-wall region.

The classical remedy to this problem is to modify the subgrid model, by means of damping functions, which provides the correct scaling of ν_k with y^+ as the wall is approached, or by using separate wall models (Fureby *et al.*, 2003). Based on our accumulated experience in high Re-number flows, we here use two different approaches:

- An explicit wall-model used together with the OEEVM, hereafter referred to as OEEVM+WM. Here, the subgrid viscosity is modified in such a way that $\nu_k=\nu+\nu_{BC}=\tau_w/(\partial v/\partial y)_P=u_\tau y_P/v_P^+$ (e.g. Fureby *et al.*, 2003) where u_τ is determined from the law-of-the-wall.
- A dynamic subgrid model using the localized dynamic approach (Kim & Menon, 1994 and Kim & Menon, 1999) used in conjuction with SMG, and hereafter referred to as LDSMG. This model utilizes the scale-similarity found between **B** and $\mathbf{L}=(\overline{\overline{\mathbf{v}}\otimes\overline{\mathbf{v}}}-\overline{\overline{\mathbf{v}}}\otimes\overline{\overline{\mathbf{v}}})$ (Liu, 1994) and between the dissipations at the subgrid and test filter levels, respectively, to estimate (in the least-square sense) the values of the model coefficients c_I or c_D, and c_k and c_e if based on the OEEVM.

NUMERICAL METHODS

A finite volume method (e.g. Hirsch, 1999) for arbitrary cell-shapes and a segregated approach described by Jasak (1997) is used to discretize the LES equations. Spatial central difference interpolation with compact second order stencils based on the Gauss theorem, and time integration performed by explicit, second order backward differencing, guarantee overall second order accuracy of the solution and low numerical diffusion. The pressure-velocity coupling is handled with a PISO procedure based on a modified Rhie-Chow interpolation for cell centered data storage. This method results in a CFL-number restriction; A maximum CFL number of 0.5 gives adequate stability, but a CFL number of 0.3 is used since LES attempts to resolve the dynamics of the large scales.

RESULTS

To compare the simulations with the experimental data, a set of sample rakes and planes are chosen: cross-sectional planes at locations (i) x/L=0.600 and (ii) x/L=0.772; a circumferential line along the median of the ellipsoid body; Two sampling rakes in each of the planes (i) and (ii), extending from the hull surface 20 mm along the surface normal at 130° and 90° from the leeward center line respectively. Pressure, velocity, secondary streamlines and surface flow patterns in the above groups are used as base for the validation. Furthermore, flow visualisations using streamlines and contour plots help analyze the complexity of the flow pattern. Table 1 presents an overview of the simulations carried out.

Table 1: Scheme over selected run configurations.

Run	α	*Grid*	*LES mod*	*Wall mod*
I	10	A	OEEVM+WM	Log-law
II	20	A	OEEVM+WM	Log-law
III	20	B	OEEVM+WM	Log -law
IV	20	A	OEEVM	van-Driest
V	20	A	LDSMG	–
VI	20	C	LDSMG	–

General Observations and Flow Physics

The computational results reveal a plethora of complex three-dimensional flow features. These include stagnation flow, three-dimensional boundary layers under influence of pressure gradients and streamline curvature, cross-flow separation and the formation of free vortex sheets ensuing streamwise vortices. Such features are archetypes of flows around airborne and underwater vehicles warranting an in-depth study. On the windward portions of the body a stationary attached flow is observed whereas after separation, and particularly under the vortex systems, intense fluctuations in the flow are found. The differences in the overall flow pattern between the LES models are few, but variations in separation location, vortex position and boundary layer profiles occur as is discussed below.

The streamribbons of figure 1 clearly show the complexity of the flow for α=10° and α=20°, respectively. On the windward side, an attached 3D boundary layer is formed, whereas on the leeward side the circumferential adverse pressure gradient causes the flow to detach from the hull and roll up into a counter-rotating vortex pair, spiraling along the back of the body. A closer inspection of the α=20° case results reveals a secondary vortex located very close to the hull surface just below each primary vortex. This weak vortex structure is quickly (and intermittently) enrolled in the primary vortex as can be seen in the upper panel of figure 1.

For α=10°, the primary vortex system stays close to the hull along the entire body, but at α=20° the primary vortices detaches from the boundary layer fairly early. At the cross-section x/L=0.600, the primary vortex is flat and located very close to the hull whereas in a cross-section at x/L=0.772 it has detached completely from the hull and increased considerably in strength. Figure 3 shows the differeces in vortex developement in terms of secondary streamlines superimposed on the resolvable turbulent kinetic energy $k=\frac{1}{2}\langle(\overline{\mathbf{v}}-\langle\overline{\mathbf{v}}\rangle)^2\rangle^{1/2}$ and the axial velocity. For α=10° and x/L=0.600 neither experiments nor LES show true vortices (defined by closed streamlines), but instead a sheet of fluid rolling-up. At x/L=0.772 both experiments and LES show true vortices at around $\varphi\approx$145° and about 1.3 cm above the body surface. For α=20° and x/L=0.600 the primary vortex is at $\varphi\approx$150° and 1.7 cm above the hull. At x/L=0.772 the primary vortex is at $\varphi\approx$152° and 3.2 cm above the body surface. For α=20° a secondary vortex is found close to the body at $\varphi\approx$140° at the aft cross-section.

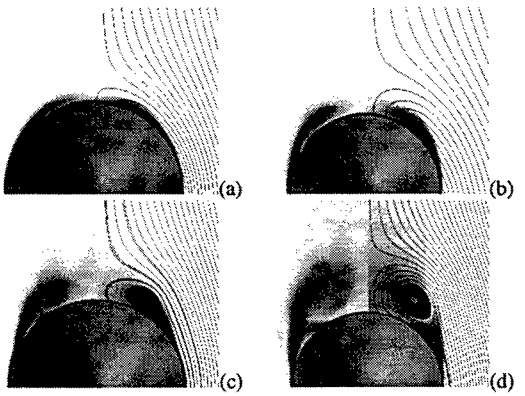

Figure 3. Secondary streamlines superimposed on contours of k (left) and on U (right) for the OEEVM+WM. (a) α=10° and x/L=0.600, (b) α=10° and x/L=0.772, (c) α=20° and x/L=0.600, (d) α=20° and x/L=0.772.

In figure 4 we show the surface flow field for α=10° and 20°. At α=10° the surface streamlines converge from the windward side to the leeward side forming a free-vortex type separation identified by surface stremlines merging together along a line and leaving the surface along it. Detachment is accompanied by the formation of the longitudinal spiraling vortices, figure 1b. It is interesting to note the downward deflection of the streamlines on the hull, suggesting a reversal of the circumverential velocity component. At α=20° we find a second open separation supporting the two almost parallel pairs of longitudinal spiraling vortices seen in figure 1b. A small region of flow reversal is found at the rear end of the spheroid. In general we find that in addition to form a second open separation the increased angle of attack forces the primary line of open separation to move upstream. The features displayed and described here are in good agreement with the visualization study of Han & Patel (1979).

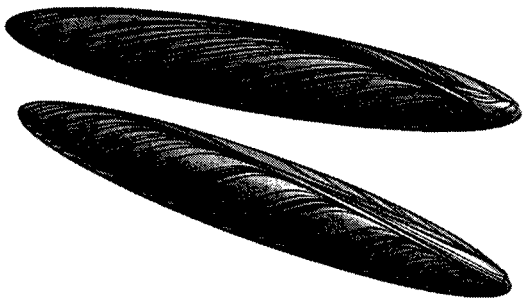

Figure 4. Predicted surface flow pattern for the α=10° case (upper panel) and the α=20° case (lower panel).

Detailed Comparisons of Pressure and Velocity

In figure 5a we show the static pressure coefficient C_P where $C_P=2(\langle p\rangle-p_0)/v_0^2$ in which p_0 is a reference pressure, in the meridian plane. For α=10° the agreement between LES and experimental data is generally good, especially on the leeward side. On the windward side, in the aft region, there is some discrepancy, possibly related to the presence of the support sting used in the experiments but not included in the LES'. For α=20° no experimental data exists, but good agreement is found between the different LES'. In figure 5b, C_P is shown as function of φ (the azimuthal angle measured from the symmetry plane on the windward side of the body) at x/L=0.772. For α=10° the agreement between LES and experimental data is good with the exception of the sector between φ=120° and 150°. This corresponds to the region beneath the primary vortex, cf. figure 3, and from theoretical considerations we expect a low-pressure patch on the hull beneath that vortex. For α=20°, C_P shows the existence of both a primary and a secondary separation on the body and the agreement between experimental data and LES is good for runs I-III, especially on the windward side. The LDSMG predictions are somewhat different, and the fine grid results suggest an early separation at $\alpha\approx$100°.

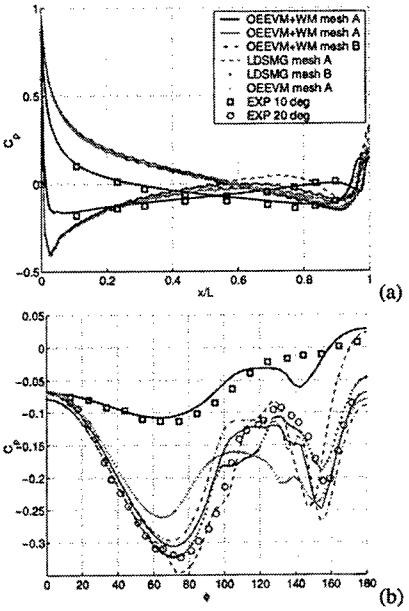

Figure 5. Comparison of the static pressure coefficient, C_P, at (a) the meridian plane and (b) x/L=0.772.

Figure 6 shows the normalized time-averaged, velocity components (U,V,W) in the body coordinate system along the two sample rakes for α=10° and 20°, respectively. Here, U is tangent to the body pointing towards the tail, V is normal to the body (positive outwards) whereas W is orthogonal to both U and V. Considering first the results obtained on grid A we find that the OEEVM+WM gives best agreement between predictions and experiments followed by the LDSMG, whereas the OEEVM shows a less satisfactory agreement. OEEVM overpredicts U and W in the outer part of the boundary layer at x/L=0.600 and underpredicts U and W in the entire boundary layer at x/L=0.772. This is likely to be caused by insufficient resolution of the inner part of the boundary layer, which is taken care of by the wall-model in the OEEVM+WM and the dynamic procedure in the LDSMG – enforcing proper near wall-scaling. The results from the OEEVM+WM appaers virtually unaffected by the resolution, cf runs II and III. The LDSMG model on

the other hand, clearly appears more sensitive to the resolution, as can be seen in figures 5-8, and the finer mesh produces a thinner boundary layer, and a contraction of the vortices toward the hull.

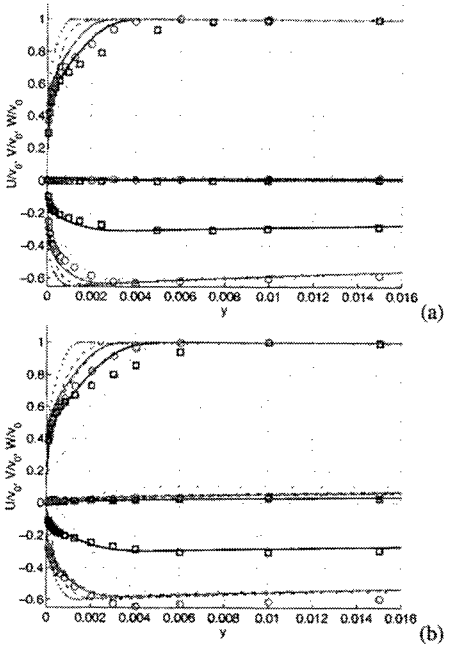

Figure 6. Comparison of the normalized velocity (U,V,W) in the body surface coordinate system at (a) x/L=0.600, φ=90° and (b) x/L=0.772, φ=90°. Note that the results and data for the α=10° case are shifted one unit in the ordinate direction. For legend see figure 4.

The different subgrid and wall-models show that the choice of LES model and the associated wall treatment is important when complex flows are considered. Differences in boundary layer thickness and vortex positions are obvious between e.g. run II and V as evident in figures 5b and 6. All models, however, predict a thinner boundary layer than found in the experimental data. This puzzles the authors, as the inner part of the bounday layer is well captured in most cases. The reason for this discrepancy is not fully understood, but may stem from background turbulence levels or from the fact that the outer boundary layer is sensitive to the exact location of vortex systems and separation points. Another source of discrepancy may stem from the mentioned trip-wire used to trigger turbulence in the experiments. No such device is incorporated in the simulations.

Figure 7 shows secondary streamlines superimposed on U for runs II (left) and III (right) at x/L=0.600 (a) and x/L=0.772 (b), whereas figure 8 shows secondary streamlines superimposed on U for runs V (left) and VI (right) at x/L=0.600 (a) and x/L=0.772 (b). These comparisons show a difference in mesh sensitivity between the OEEVM+WM model and the LDSMG model. LDSMG seems to be sensitive to the resolution, while the OEEVM+WM is almost independent of the refinement between meshes A and B. A more thorough grid convergence study is needed to investigate these observations further.

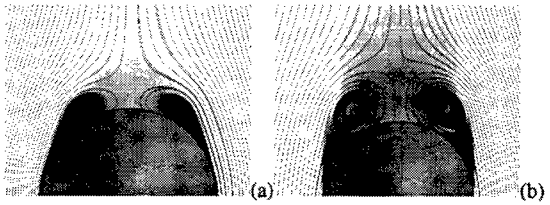

Figure 7: Vortex development in case II (left) and III (right). Secondary streamlines superimposed on U at x/L=0.600 (a) and x/L=0.772 (b).

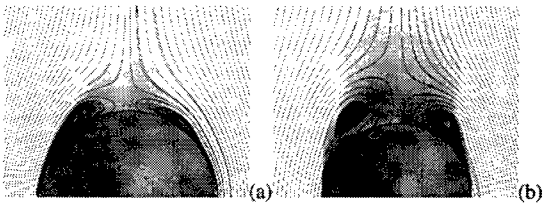

Figure 8: Vortex development in case V (left) and VI (right). Secondary streamlines superimposed on U at x/L=0.600 (a) and x/L=0.772 (b).

CONCLUDING REMARKS

The application of LES to complex wall-bounded flow requires time-consuming validation of the model on non-trivial flows such as the prolate spheroid. All configurations tested show good qualitative results, but predict different lines of separation, vortex locations and boundary layer shapes and hence also different hull pressure distribution. The boundary layer was generally too thin, the reason to which the authors have no clear explanation, but allude to background turbulence level and the differences between the experimental and computational setups. Nevertheless, it is notable that the inner parts of the boundary layer were well captured by most of the models, even at locations near separation lines and below the complex vortex system.

Of the models tested, the OEEVM with a law-of-the- wall based near-wall model shows the most promising result when compared to experimental data. The dynamic model shows promising results but a more severe grid dependency that implies further grid convergence studies. The OEEVM with van-Dreist damping is shown to predict the poorest results. Other models than the above presented were tested in the study of this flow case, e.g. Monotonely Integrated LES (MILES) (Fureby & Grinstein, 2002). These however, tended to produce too week subgrid viscosity and rendered somewhat thiner and more violent boundary layer.

ACKNOWLEDGEMENT

These computations were performed with an earlier research version of the FOAM code (Weller *et al.*, 1997) for further details see http: //www.nabla.co.uk.

REFERENCES

Chesnakas C.J. & Simpson R.L.; 1996, "Measurements of Turbulence Structure in the Vicinity of a 3D Separation", J. Fluids Eng., **118**, p 268.

Constantinescu G.S., Pasinato H., Wang Y.-Q., Forsythe J.R. & Squires K.D.; 2002, "Numerical Investigation of Flow past a Prolate Spheroid", AIAA 02-0588

Ferziger J.H.; 1983, "Higher Level Simulations of Turbulent Flows", in Computational Methods for Turbulent, Transonic and Viscous Flows, Oxford University Press, Oxford, Ed J.-A. Essers.

Fureby C. & Grinstein F.F.; 2002, "Large Eddy Simulation of High Reynolds-Number Free and Wall Bounded Flows", J. Comp. Phys., **181**, p 68.

Fureby C., Alin N., Wikström N., Menon S., Persson L., & Svanstedt N.; 2003, "On Large Eddy Simulations of High Re-number Wall Bounded Flows", AIAA Paper No 2003-0066.

Fureby C.; 2001, "Towards Large Eddy Simulation of Complex Flows, In Direct and Large Eddy Simulation IV, Eds. Friedrich R. & Rodi W., Kluwer, The Netherlands.

Germano M., Piomelli U., Moin P. & Cabot W.H.; 1994, "A Dynamic Sub Grid Scale Eddy Viscosity Model", Phys. Fluids A **3**, p 1760.

Goody M., Simpson R.L. & Engel M.; 1998, "Mean Velocity and Pressure and Velocity Spectral Measurements within a Separated Flow Around a Prolate Spheroid at Incidence", AIAA Paper 98-0630.

Weller H., Tabor G., Jasak H., & Fureby C.; 1997, "A Tensorial Approach to CFD using Object Oriented Techniques", Comp. in Physics, **12**, p 699.

Han T. & Patel V.C.; 1979, "Flow Separation on a Spheroid at Incidence", J. Fluid Mech. **92**, p 643.

Hedin, P.-O., Alin, N., Berglund, M. & Fureby, C.: 2001, "Large Eddy Simulation of the Flow Around an Inclined Prolate Spheroid", AIAA Paper 01-1035.

Hirsch C.; 1999, "Numerical Computation of Internal and External Flows", J. Wiley & Sones.

Jasak H.; 1997, "Error Analysis and Estimation for the Finite Volume Method with Application to Fluid Flows", PhD thesis, Imperial College, London, UK.

Kim W.-W. & Menon S.; 1994, "A New Dynamic One Equation Sub Grid Scale Model for Large Eddy Simulations", AIAA Paper No 95-0356.

Kim W.-W., & Menon S.; 1999, "A new Incompressible Solver for Large-Eddy Simulations", Int. J. Num. Fluid Mech., **31**, p 983.

Liu S., Meneveau C. & Katz J.; 1994, "On the Properties of Similarity Subgrid-Scale Models as Deduced from Measurements in a Turbulent Jet", J. Fluid Mech., **275**, p 83.

Rhee S.H. & Hino T.; 2000, "Computational Investigation of 3D Turbulent Flow Separation around a Spheroid using an Unstructured Grid Method", J. Soc. Naval Architects of Japan, **188**, p 1.

Sagaut, P.: Large Eddy Simulation for Incompressible Flows, Springer Verlag, Heidelberg, 2001.

Schumann U.; 1975, "Subgrid Scale Model for Finite Difference Simulation of Turbulent Flows in Plane Channels and Annuli", J. Comp. Phys., **18**, p 376.

Smagorinsky J.S.; 1963, "General Circulation Experiments with Primitive Equations", Mon. Weather Rev. **94**, p 99.

Tsai C.-Y. & Whitney A.K.; 1999, "Numerical Study of Three-Dimensional Flow Separation from a 6:1 Ellipsoid", AIAA 99-0172.

Wetzel T.G., Simpson R.L. & Chesnakas C.J.; 1998, "Measurement of Three-Dimensional Crossflow Separation", AIAA.J. 36, p 557.

Wilcox D.C.; 1998, "Turbulence Modelling for CFD", DCW Industries